JOURNAL OF PROPULSION AND POWER
Vol. 24, No. 1, January–February 2008

Numerical Simulation of Transverse Injection of Circular Jets into Turbulent Supersonic Streams

A. T. Sriram* and Joseph Mathew†
Indian Institute of Science, Bangalore 560 012, India

DOI: 10.2514/1.26884

The flowfields arising from transverse injection of sonic air jets through circular holes on flat plates into supersonic streams have been computed. Favre-averaged Navier–Stokes equations for compressible flow coupled with k–ω equations were solved with a finite-volume method. The approximate Riemann solver due to Roe has been used for obtaining inviscid fluxes at cell interfaces, with monotone upwind schemes for scalar conservation laws preprocessing for high resolution and a multistep Runge–Kutta method for time integration to steady states. A detailed comparison has been made with recent laser Doppler velocimetry measurements of velocity and turbulence kinetic energy on the symmetry plane and two crossflow planes. Wall pressures were compared with those obtained with pressure-sensitive paint from the same experimental facility. Wall pressures and features at higher crossflow Mach numbers were examined by simulating a second set of experiments. Computations capture various flow features and show very good qualitative agreement with both sets of experiments. Quantitative agreement is very good in the upstream regions and close to the jet. Small differences appear in the downstream portion as the jet develops. The changes in flow structure with increasing injection pressure suggested by sketches of oil flows are also obtained in the simulations.

Introduction

COMPLEX turbulent flows comprising three-dimensional shocks, vortices, and flow separation appear in several aerospace applications. As computing power increases, numerical predictions of such flows have become more feasible and therefore play an increasing role in analyses and design. Reliable predictions of detailed flowfields allow better assessment of new ideas in such sensitive flows as those in scramjet engines. It is not sufficient that global parameters alone are computed with good accuracy. The local solutions must also be accurate enough if, for example, new ideas for improved mixing are to be assessed. The subject of the present study is an examination of the accuracy of predictions of general, compressible, turbulent mean flows using a widely applied numerical model. The flow considered arises when a jet is injected transversely through a circular port into a supersonic stream. Detailed flowfield data (velocity components) over the longitudinal midplane and two crossflow planes from the laser Doppler velocimetry (LDV) measurements of Santiago and Dutton [1,2] have become available recently, making detailed comparisons of the interior flowfields possible. Earlier, in these sensitive, supersonic flows, only wall data could be examined quantitatively. Here, the full set of conservation laws were solved in a coupled manner using Roe's approximate Riemann solver and monotone upwind schemes for scalar conservation laws (MUSCL) preprocessing as discussed here, and turbulence was modeled using a two-equation k–ω model. Comparisons show that the numerical predictions are quite accurate over most of the flow. Differences appear in the region occupied by the deflected jet, which is likely to be due to the low-frequency/large-scale unsteadiness in the jet's development.

We consider a uniform, turbulent, supersonic flow over a flat plate with a circular port through which a highly underexpanded jet is injected. Figure 1 is a sketch of the main flow features. The Cartesian coordinate system used has the x axis aligned with the incoming supersonic stream, the y axis is normal to the plate, and the z axis is in the spanwise direction. The origin is on the axis of the injector, $y = 0$ is the plate surface, $z = 0$ is the symmetry plane, and $x = \text{const}$ on crossflow planes.

The jet expands rapidly about the lip. Expansion waves reflect from the jet boundary as compression waves and coalesce as a barrel shock connected to a Mach disk. The jet is deflected downstream due to the crossflow and develops a kidney-shaped cross section. The flow in any cross-sectional plane of the jet is roughly that due to a pair of counter-rotating, streamwise-oriented vortices. The sense of rotation is that imparted by the higher speed flow of the incoming stream, which travels around the jet. Ahead of the jet there is a bow shock, separated flow, and a mild separation shock. The obstacle presented by the round jet is localized, and the main stream travels around the jet. So the bow shock is curved around the jet as also the upstream separation zones. There are separation zones downstream, beneath the jet, which present a more complicated nested structure.

This configuration has been the subject of many experimental studies. Zukoski and Spaid [3] studied pressure and concentration fields and shock shape. Penetration height was recognized as the single most important parameter for scaling. They showed that the upstream separation length is considerably larger when the incoming boundary layer is laminar than when it is turbulent. Schetz et al. [4] studied the structure of the jet and found the downstream displacement of the center of the Mach disk from the injector to be nearly equal to its distance from the plate. These early experiments were conducted to provide simple relations for design purposes. Supersonic flows are quite sensitive, and intrusive measurements can alter the flow considerably. So measurements have usually been of wall static pressure only. Recently, detailed measurements of the interior fields have become available from a sequence of studies. They include qualitative studies of flow features using planar laser-induced flourescence (PLIF) and Mie scattering [5], quantitative velocity, and turbulent field data using LDV [6] and wall pressure distribution with pressure-sensitive paint (PSP) [7]. Many aspects were studied, such as mixing and penetration, the presence of shear layer vortices at the jet/freestream interface [5], bow shock and jet interaction [8], compressibility effects, wake vortices [9], and crossflow vortices [1]. Among these, the results of Santiago and Dutton [1] and Everett et al. [7] have been used in the present work for detailed quantitative comparisons and assessments of the computations. Simulations of a second set of experiments, namely,

Received 21 August 2006; revision received 25 July 2007; accepted for publication 26 July 2007.

*Ph.D. Student, Department of Aerospace Engineering.
†Associate Professor, Department of Aerospace Engineering. Associate Fellow AIAA.

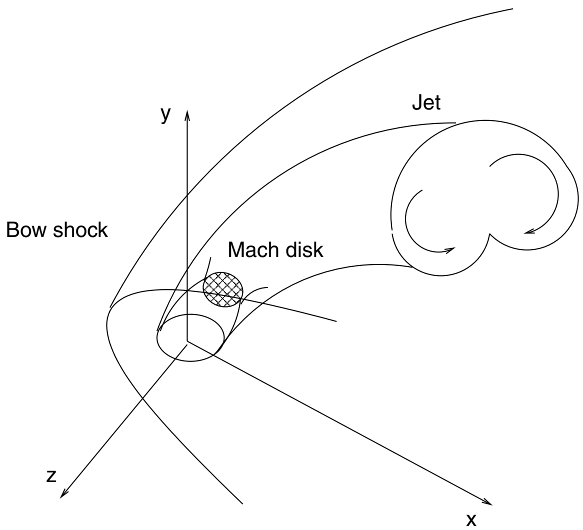

Fig. 1 Flow structure near injection port.

those of Aso et al. [10], who provided wall pressure distributions and very interesting oil flow visualizations, are also presented here.

Drummond [11] has reviewed computational fluid dynamics (CFD) techniques relevant to scramjet simulations. Most early calculations were performed with the MacCormack method and Baldwin–Lomax model for turbulence. Segal et al. [12] simulated transverse injection ahead of a backward-facing step to determine the influence of upstream separation on fuel mixing and flame holding. Mao et al. [13] used a parabolized Navier–Stokes solver to compute the downstream development of the jet. An experiment that recorded the spanwise spreading of fuel in the jet [14] was simulated by Uenishi and Rogers [15]. The main objective of these early simulations was to obtain global quantities of engineering interest rather than details of the flowfields and insight therefrom. The experiments of Aso et al. [16] showed changes in flow patterns near the wall as injection pressure was varied. They also reported their own computations with the Harten–Yee scheme and Baldwin–Lomax model. Wall static pressures at several points along lines in the streamwise direction along the center line and at spanwise distances of $1d$, $2d$, and $4d$ were compared (d is the hole diameter), and a good agreement was noted. Both measurement and simulation showed a dip in the upstream portion at a spanwise distance of $2d$. This was interpreted as being due to the presence of a horseshoe vortex, and supporting sketches of their oil flow visualization were included. Total pressure over a transverse plane was also compared. Mach number contours on the symmetry plane and particle paths around the jet from the computations have been shown. A comparison of oil flow visualization with computed wall shear stress field would have been useful.

Most of the earlier computations used the Baldwin–Lomax turbulence model. This model is calibrated for the flow over a flat plate on which the inner and outer region structure is reasonable. The transverse jet has a more complex turbulence structure with different-length scales in the near-wall regions and over the jet's counter-rotating vortices. The two-equation models are more appropriate for this flowfield because the variation in scales at the different regions are obtained directly when the equations for turbulence kinetic energy and a second quantity (ϵ or ω) are solved. Apart from using better turbulence models, comparisons of interior flowfields with experiments are needed to asses the prediction. Such a comparison has been reported recently by Maddalena et al. [17]. They conducted experiments and computations of helium injections into a Mach 4.0 air crossflow. The computations used Wilcox's k–ω model with a Roe scheme and are quite similar to our method. They compared fields of total temperature, pressure, mass fraction, and Mach number 16-hole diameters downstream. They found the mixing predictions to be inaccurate. There are some salient differences from our study, but some observations are consistent with ours. We have examined only the near-field development as far as five diameters downstream of the hole. We found differences in the jet development rate compared with the experiment, whereas the injector near field is quite accurate. There is an unsteadiness in the jet, which the turbulence model does not take into account. It is possible that this effect is more severe in Maddalena et al. [17] because the comparisons are much farther downstream. Moreover, they observed different levels of inaccuracies with different injectors. It would be useful to document the large-scale unsteadiness because it can have a significant effect on mean distributions.

To the best of our knowledge, there are no other detailed comparisons of the interior distributions reported, perhaps because such measurements [2,7] have become available only recently. In this study, a widely used, complete turbulence model, a two-equation k-ω model with suggested compressibility corrections, was used. Although it may be worthwhile to examine even more sophisticated models such as a Reynolds stress model, we have restricted this study to a two-equation model because it appears to be the level of modelling being used in applications at this time. Moreover, our experience [18] with the two-dimensional counterpart of this flow, the transverse injection of plane jets through slots, suggests that accurate, reliable solutions can be obtained with the k–ω model.

Reference Experiments

Earlier experiments [3,4] were conducted to identify scaling parameters and to obtain empirical laws for design. Recent experiments have the newer aim of validating computations of this type of flow. Table 1 lists flow conditions in the experiments, which have been simulated here. Notably, these experiments are from two different tunnels with considerable differences in freestream Mach number.

The first set of four experiments (cases 1–4 in Table 1) were conducted in a rectangular blowdown wind tunnel, and a sonic jet of air was injected from a tunnel wall. The test section was 754 mm long, and extended from a two-dimensional supersonic nozzle, which provided a Mach number of 1.6 in the test section. Inflow stagnation pressure and stagnation temperature were $p_{0\infty} =$ 241 kPa and $T_0 = 295$ K, respectively. The test section height was 36 mm, and the width was 76 mm. A convergent axisymmetric nozzle was used to inject the sonic jet of air through a 4-mm-diam (d) circular port at a total pressure of 476 kPa and stagnation temperature of 295 K. The port was located in the fully turbulent boundary layer where the thickness was approximately equal to the nozzle diameter. Boundary layer properties, 20 mm upstream of port center, were measured. The boundary layer, displacement, and momentum

Table 1 Conditions in experiments. The variable $\dot{m}_{\text{jet}}$ is the theoretical mass flow rate, and $J = \rho_{\text{jet}} u_{\text{jet}}^2 / \rho_\infty u_\infty^2$ is the momentum flux ratio

Case	M_∞	p_∞, kPa	T_∞, K	T_{jet}, K	$\frac{p_{\text{jet}}}{p_\infty}$	$\dot{m}_{\text{jet}}$, kg/s	J
1	1.60	56.7	198.4	250	4.43	0.0140	1.73
2	1.60	56.7	198.4	250	3.07	0.0097	1.20
3	1.60	56.7	198.4	250	4.36	0.0137	1.70
4	1.60	56.7	198.4	250	5.65	0.0178	2.21
5	3.75	11.1	78.69	250	8.57	0.0082	0.61
6	3.75	11.1	78.69	250	17.72	0.0170	1.26
7	3.75	11.1	78.69	250	26.29	0.0253	1.87

thicknesses were 3.1, 0.59, and 0.26 mm, respectively. Friction velocity was 16.8 m/s. The analytical expression of Sun and Childs [19] is a good fit to the measured velocity profile. The experiments of Santiago and Dutton [2] from this facility provide LDV data on the symmetry plane and two crossflow planes across the jet as it develops downstream. (case 1 in Table 1). At approximately the same conditions, Everett et al. [7] recorded wall pressure measurements with PSP (case 3 in Table 1). Hence the cases 1 and 3 together serve as a complete set of data for code validation. Cases 2–4 provide wall pressure data at different injection pressures.

The second set of three experiments (cases 5–7 in Table 1) were reported by Aso et al. [10], who mounted a 150 mm-wide flat plate with a sharp leading edge in a supersonic wind tunnel of 150×150 mm cross section. A circular nozzle was located at a distance of 300 mm from the leading edge. Nozzles of diameters 3 and 5 mm were used. Nitrogen was injected at sonic conditions into the air stream. Experiments were conducted at freestream Mach numbers of approximately 3.75–3.81, at a total pressure of 1.20 MPa, and at total temperatures of approximately 283–299 K. The Reynolds number based on distance from the leading edge of the plate to the injection location varied from $1.03–2.07 \times 10^7$. Schlieren visualization of the shock structure and oil flow visualization on the plate were done. Surface pressure was measured from ports located along several lines at constant spanwise distances from the injection port.

Numerical Method

Governing Equations

The governing equations consist of the Navier–Stokes for Favre-averaged mean fields of compressible, turbulent flows, an equation of state, and other constitutive relations (see, for example, Wilcox [20]). The compressible form of the k–ω equations are solved simultaneously to provide turbulence modeling. The transport equations have the form

$$\frac{\partial U}{\partial t} + \frac{\partial F}{\partial x} + \frac{\partial G}{\partial y} + \frac{\partial H}{\partial z} = S$$

where $U = [\rho, \rho u, \rho v, \rho w, \rho E, \rho k, \rho\omega]^T$ is a vector field of the state variables, F, G, and H are flux vectors consisting of both inviscid and viscous parts, and S is a source vector. The velocity components are u, v, and w in x, y, and z directions, respectively, ρ is the density, and total energy is $E = e + \frac{1}{2}(u^2 + v^2 + w^2) + k$. The energy $e = c_v T$ and the perfect gas equation of state $p = \rho R T$ was used. The turbulence kinetic energy is represented by k, and ω is the specific dissipation rate. The effective viscosity is taken as the sum of the molecular and eddy viscosities, $\mu_{\text{eff}} = \mu + \mu_t$, where $\mu_t = \rho k/\omega$.

Turbulence Model

Confidence in a particular turbulence model is still limited to some classes of flows for which reliable and accurate results have been obtained. Because the two-equation models are complete, they are perhaps the more widely used in applications in spite of known limitations. For example, Wilcox [20] compares solutions of adverse pressure gradient flows and shows that the k–ϵ model is quite inaccurate, whereas his refinements k–ω model has provided accurate solutions. It is this model that has been used in the present study. An apparent limitation is a sensitivity of this model to freestream turbulence level. Care is needed, and has been taken here, that the solutions are not affected. In this case, the turbulence in the freestream decays and is generated at the bow shock. Processes that change the turbulence levels are driven by the injected flow, the shocks, and shear layers that are present so that the solutions do not exhibit such a sensitivity. Secondly, turbulence modeling had been developed and calibrated for incompressible flow. The special effects due to compressibility and the modeling required are being uncovered slowly. Some effects have been incorporated as explicit compressibility corrections in Wilcox's k–ω model following earlier proposals [21,22]. We used this version because of its closer prediction of shear layer growth. The effects of turbulence modeling were examined first with 2-D computations of injection through a slot [18]. It was found that turbulence modeling was not a limitation, in spite of the presence of several types of flow features, and in particular that the k–ω method was very accurate as long as the computations are of adequate resolution. The model is stated and discussed in Sec. 4.3.1 of Wilcox [20], with Wilcox's compressibility corrections in Sec. 5.5.1.

Numerical Scheme

The governing equations are cast into a standard finite volume formulation [23]. The vector U is the average over the cell. Numerical fluxes at cell interfaces were calculated using Roe's approximation to the Riemann solution [23]. Then, the inviscid part of the flux at the interface

$$F_{\text{inv},i+\frac{1}{2}} = \frac{1}{2}(F_{\text{inv},L} + F_{\text{inv},R}) - \frac{1}{2}\sum_{i=1}^{m} |\hat{\lambda}_i| \Delta V_i \hat{R}^{(i)}$$

where $F_{\text{inv},L}$ and $F_{\text{inv},R}$ are the fluxes calculated, respectively, from values in the cells to the left and right, respectively. The eigenvalues and matrix of right eigenvectors for the x-direction flux are

$$\lambda_1 = \hat{u} - \hat{c}, \qquad \lambda_2 = \hat{u}, \qquad \lambda_3 = \hat{u}, \qquad \lambda_4 = \hat{u}$$
$$\lambda_5 = \hat{u} + \hat{c}, \qquad \lambda_6 = \hat{u}, \qquad \lambda_7 = \hat{u}$$

$$\hat{R} = \begin{bmatrix} 1 & 0 & 0 & 1 & 1 & 0 & 0 \\ \hat{u} - \hat{c} & 0 & 0 & \hat{u} & \hat{u} + \hat{c} & 0 & 0 \\ \hat{v} & 1 & 0 & \hat{v} & \hat{v} & 0 & 0 \\ \hat{w} & 0 & 1 & \hat{w} & \hat{w} & 0 & 0 \\ \hat{H} - \hat{c}\,\hat{u} & \hat{v} & \hat{w} & \frac{1}{2}q^2 + \hat{k} & \hat{H} + \hat{c}\,\hat{u} & 1 & 0 \\ \hat{k} & 0 & 0 & \hat{k} & \hat{k} & 1 & 0 \\ \hat{\omega} & 0 & 0 & \hat{\omega} & \hat{\omega} & 0 & 1 \end{bmatrix}$$

where $q^2 = (\hat{u}^2 + \hat{v}^2 + \hat{w}^2)$. The $\hat{.}$ denotes the Roe-average values of the variable. The corresponding wave strengths ΔV_k are elements of the vector

$$\Delta V = [(\Delta p - \hat{\rho}\,\hat{c}\,\Delta u)/2\hat{c}^2, \hat{\rho}\Delta v, \hat{\rho}\Delta w, \Delta\rho - \Delta p/\hat{c}^2,$$
$$\times (\Delta p + \hat{\rho}\,\hat{c}\,\Delta u)/2\hat{c}^2, \hat{\rho}\Delta k, \hat{\rho}\Delta\omega]^T$$

The viscous parts of the fluxes were obtained by evaluating derivatives to second order. The other two fluxes, namely G and H, are calculated similarly. A semi-implicit version of the Runge–Kutta method [24] was used for fast convergence.

The code was validated systematically with shock-turbulence interaction problems before our previous studies. However, before performing the 3-D round-jet simulations, the analogous, two-dimensional, transverse injection through a slot was considered for further validation. Several previous numerical studies have predicted major flow features, and accurate predictions have been obtained for lower injection pressures. Measurements from experiments as well as computations by others are available for validation. A systematic study over the full range of injection pressure ratios for which measurements are available was conducted. Not only did this serve to validate our approach, but methods to obtain good predictions at high pressure ratios also could be determined [18].

Simulations of Experiments of Santiago and Dutton

Computational Domain and Boundary Conditions

In terms of the injector port diameter d, the streamwise extent was $13d$ ($-5 < x/d < 8$). The inflow plane was located $5d$ upstream of the port center because the velocity profile of the turbulent boundary layer at this location is known from the measurements. The downstream extent of $8d$ is far enough for flow development to have become uniform. The spanwise extent was $4d$ and symmetric $0 < z/d < 4$. The height was taken to be 33 mm ($8.25d$), because the test section height was 36 mm and the boundary layer thickness was 3.1 mm.

Inflow boundary conditions at $x = -5d$ were taken from a two-dimensional simulation of flow over a flat plate. The turbulent velocity profile with the required boundary layer thickness of 3.1 mm agreed well with the measured profile [2] at $x = -5d$ and also satisfied the log law. The lower wall ($y = 0$) was taken to be adiabatic. No-slip conditions were imposed for velocity, and pressure was extrapolated from interior points. The value of k was set to zero and the hydraulically smooth-surface condition was used to calculate ω. The jet conditions are the Mach number $M_{\mathrm{jet}} = 1$, temperature $T_{\mathrm{jet}} = 249$ K, and injection pressure $p_{\mathrm{jet}} = 4.43 p_\infty$. Cells near the jet boundary had a slightly lower velocity in such a way that the overall mass flux was maintained at the value in the experiment. This is an approximation to account for the representation of the curved boundary and also models the (undocumented) boundary layer flow at the injector port. At the injector, the values $k = 100$ m^2/s^2 (turbulence intensity is $\approx 1\%$) and $\omega = 5 \times 10^5$ s^{-1} were prescribed (Gerlinger et al. [25] has recommended that a value for ω be prescribed rather than taking its jet-axis derivative to be zero). On the symmetry plane ($z = 0$), the z component of velocity w vanishes. For other variables, the spanwise derivative vanishes. This is implemented by setting values in dummy cells across the symmetry plane equal to (for vanishing derivatives) or as the negative of (for w) the value in the first cell within the computational domain. At the upper wall, slip flow conditions were imposed, and the boundary layer was not resolved. It was treated as an adiabatic wall, and inviscid flow conditions were applied to reflect the shock. The other boundary planes were treated as outflow boundaries in which all the variables were extrapolated from the interior.

Grid Requirement and Convergence

Computations of the two-dimensional (slot) injection flows indicated that it is crucial to provide very good resolution of the jet between the injector exit and the Mach disk, at the least [18]. Three grids of $60 \times 40 \times 30$, $120 \times 60 \times 60$, and $180 \times 180 \times 60$ points, referred to here as coarse, medium, and fine, respectively, were considered. Grid spacing was nonuniform in all three directions. Each refinement was decided after analyzing the solution features obtained on the coarser grid. A large number of grid points in wall-normal direction were added in the fine mesh to examine whether there could be a significant effect on the solution. The grids were generated with one-dimensional stretching functions [26] that clustered points near the wall (wall-normal coordinate) and about the injection port (streamwise and spanwise coordinates).

Computations of complex flows with first-order schemes, which are generally quite diffusive, are useful starting points because they are less likely to suffer from numerical instabilities. Such solutions serve as initial conditions for computations with higher-order schemes. Higher-order schemes are also more important in three-dimensional simulations where grid refinement alone can become prohibitively expensive. Figure 2 shows the approach to the steady solution on the medium grid in terms of the maximum change in density between successive time steps scaled with the maximum initial change $\epsilon = \max|\rho^{n+1} - \rho^n| / \max|\rho^1 - \rho^0|$. Residues fell through several decades when either the first-order scheme, or the second-order scheme with minimum modulo (minmod) limiter, were used. With the third-order scheme and Van Albada limiter, the fall is less (about four decades). However, an examination of the solution shows that this lesser fall is still adequate.

The wall pressure along the line $y = z = 0$ is a suitable representative quantity for estimating the numerical accuracy because its distribution, especially upstream of the injector, depends on where the upstream separations and shock structures are found. Figure 3 shows computed wall pressure on the medium grid with the three schemes. As may be expected, the second-order scheme finds a sharper pressure rise immediately ahead of the injector compared with the first-order scheme. The extent of the upstream separation region is also larger. The third-order scheme does not provide a discernible improvement here.

Figure 4 shows the sensitivity of predicted wall pressure distribution for the three grids. The differences between solutions on the coarse and medium grids are quite small. Even on the fine grid with substantially more points, the differences remain small. Thus it was concluded that the second-order scheme on the medium grid would be adequate.

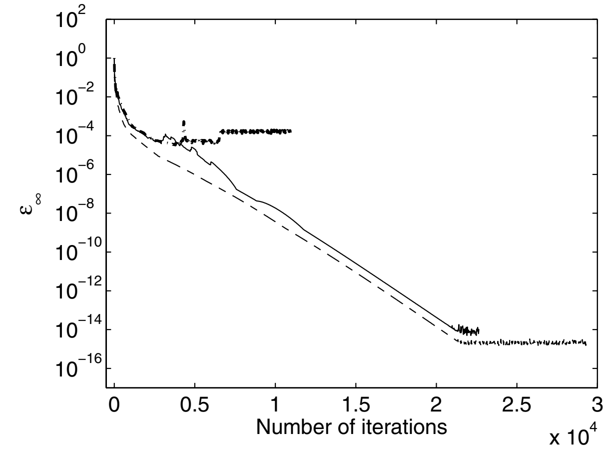

Fig. 2 Scaled residue history in L^∞ of ρ for schemes of different orders on the medium grid. Dashed line: first-order; solid line: second-order MUSCL with minmod limiter; dash-dotted line: third-order MUSCL with Van Albada limiter.

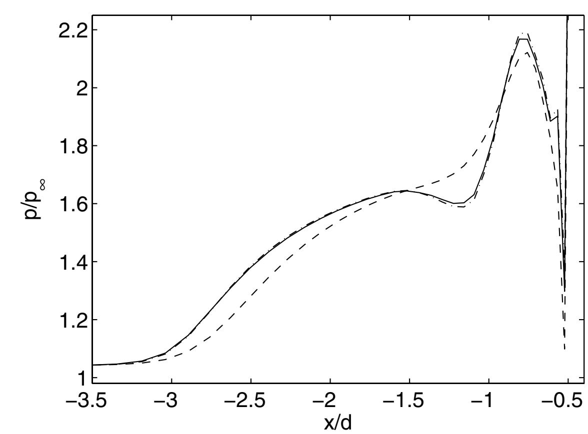

Fig. 3 Comparison of wall pressure distribution on 120 × 60 × 60 grid. Dashed line: first-order scheme, solid line: second-order scheme, dash-dotted line: third-order scheme.

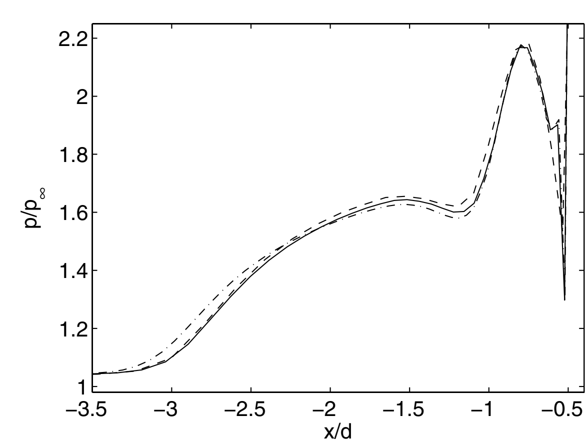

Fig. 4 Effect of grid refinement on wall pressure along plate centerline ($y = z = 0$). Dashed line: 80 × 40 × 30 grid points; solid line: 120 × 60 × 60 grid points; dash-dotted line: 180 × 180 × 60 grid points.

Comparisons with Measurements

Measurements have been taken of the wall pressure along the centerline ($y = 0$, $z = 0$) and velocity on the symmetry plane ($z = 0$)

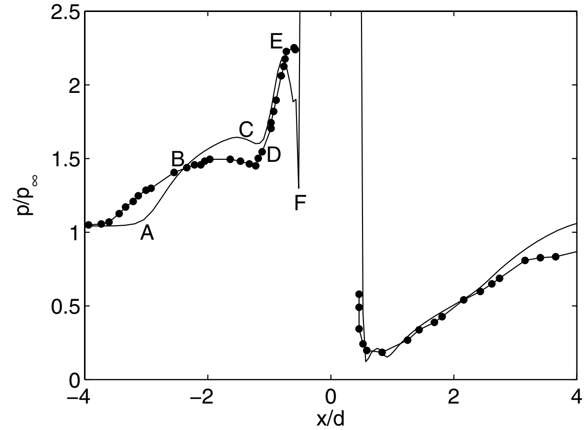

Fig. 5 Wall pressure distribution on 120 × 60 × 60 grid for case 3. Dotted line: experiment [7]; solid line: second-order scheme.

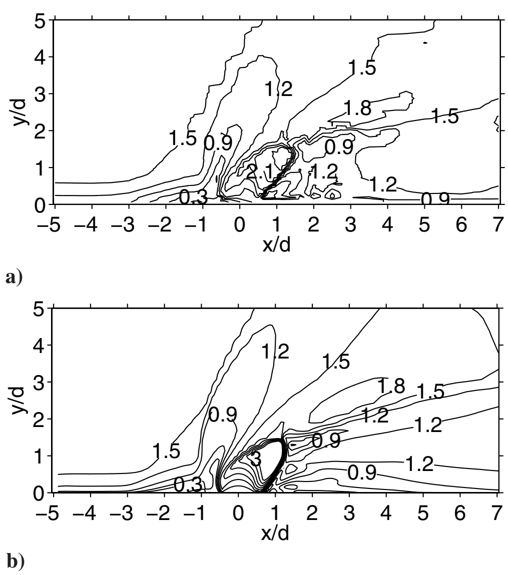

Fig. 6 Mach number contours on symmetry plane. a): experiment; b): computation.

and two transverse planes ($x/d = 3, 5$). PSP and sketches of oil flow on the wall ($y = 0$) are also available. The following discussion considers each of these data in turn.

Figure 5 shows the distribution of wall pressure on the line ($y = z = 0$) for case 1. The pressure rises in two distinct stages, labeled A–D and D–E on the computed solution. In computations, the initial pressure rise is moved downstream and is steeper, but the second stage, D–E, agrees closely with the measurement. Downstream, the agreement is very close until $x/d \approx 3$.

To relate the pressure changes, it is useful to examine the flowfield in the plane $z = 0$. From velocity measurements, and by using common reservoir conditions of injectant and crossflow fluids, Santiago and Dutton [1] provided isentropic Mach number distributions (Fig. 6a). The distribution from the computation is shown Fig. 6b. Overall, there is good quantitative agreement, especially upstream of the jet. Gradients of Mach number are smaller in the experiments, and flow structures such as jet boundary shear layers are more diffuse. The computed distribution is smooth and regular, whereas contours drawn from measurements are irregular. Diffuse structures suggest flow unsteadiness.

Salient features such as the upstream separation shock, bow shock, the turning of the jet, and the subsonic pocket downstream of the small normal shock (Mach disk) are all captured well. The injected fluid expands to a higher Mach number in the computations (about 3.1, compared with 2.4 in experiments). So the Mach disk is a stronger shock, and the downstream flow begins from a smaller

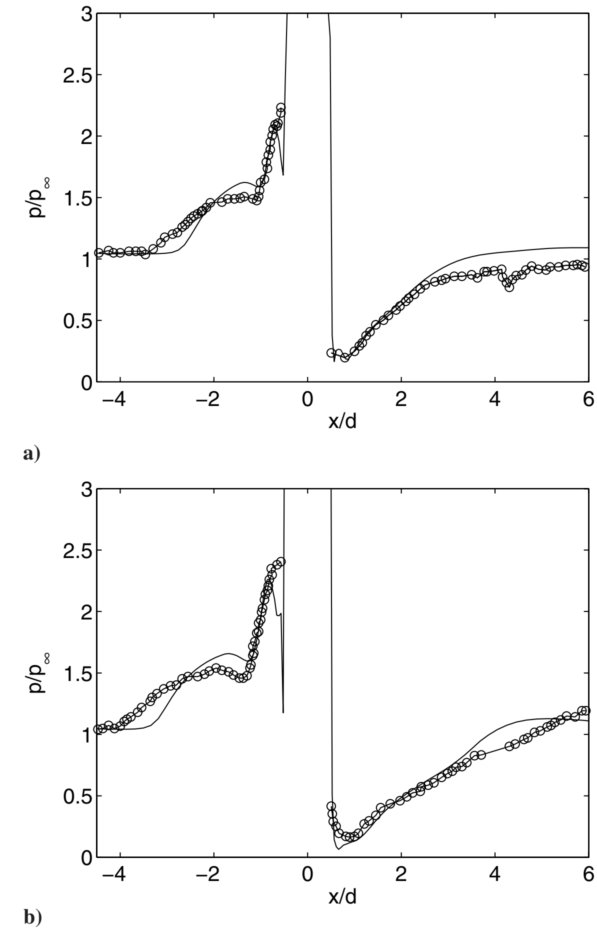

Fig. 7 Wall pressure prediction $M_\infty = 1.6$. Open-circled line: experiment [7]; solid line: computation. a) case 2; b) case 4 of Table 1.

subsonic level. The subsonic region persists in the computed jet whereas it is not present beyond about $x = 4d$ in the measurements. The initial jet boundary is nearly vertical for about $0.5d$ and then bends into the crossflow. The curvature at the windward side is slightly more than in the experiments. The location of the Mach disk has long been considered the most important measure of jet penetration which is used in simpler analyses. The measured location was $x = 1.5d$, and it is about $1.5d$ in the computation also. The farthest point on the Mach disk (from the plate) is about twice the incoming boundary layer thickness. On the leeward side, the computation shows supersonic flow just outside the barrel shock whereas in the experiment the supersonic region begins slightly further downstream.

The foot of the bow shock is at about $x = 1d$ and $y = 0.7d$. Bow shock location is slightly smeared in the experiment, perhaps due to a slight unsteadiness. Santiago and Dutton [1] interpreted the slightly sharper barrel shock on the leeward side compared with the windward side to be due to windward-side unsteadiness. However, this difference persists in the present *steady flow* computations.

The center of the primary upstream vortex is at $x = -1.15d$, $y = 0.17d$ (about $x = -1.25d$, $y = 0.13d$ in the experiment), and that of the secondary vortex is at $x = -0.625d$ and $y = 0.175d$. These structures wrap around as horseshoe vortices. The measurement shows one vortex.

Wall pressure distributions for cases 2 and 4 of Table 1 have been plotted in Fig. 7.

Perhaps further refinement and redistribution may provide closer agreement of the upstream separation and plateau pressure level but was not pursued in this study due to computational costs. We note that, unlike in slot injection flow in which predictions deviated monotonically with increasing injection pressure [18], present simulations of hole injection cases show about same level of underprediction on upstream separation length. Also, the comparison of the flowfield over the symmetry plane must be considered a more favorable assessment of the computations than that of the wall pressure on the centerline.

Mean Turbulence Quantities on Symmetry Plane

The turbulence kinetic energy distribution (TKE) on the symmetry plane shows some features of fundamental interest like turbulence amplification across shocks, large values in high shear regions, and low values in essentially inviscid regions. While discussing the TKE distribution obtained from their measurements, Santiago and Dutton [2] noted that the core of the emerging jet had very low levels of TKE, whereas higher values occurred in the shock separated regions. The bow shock could be recognized readily due to turbulence amplification across the shock.

TKE is a primary variable in the present computations. Figure 8 shows contours of TKE normalized with the square of the inflow velocity. Contour levels 0.0001, 0.001, 0.005, 0.02, 0.03, and 0.08 have been selected to show features more clearly. TKE increases at the center of the primary upstream recirculation zone to about 0.03 due to large shear. Agreement with the experiment is very close in this region. In experiments, unsteadiness was observed near the bow shock where the fluid encounters large shear, and the turbulence kinetic energy measured was about 0.08. The predicted value in this region is about the same. The core of the emerging jet shows very low values in experiment and computation, essentially like a inviscid core. At the Mach disk region, the computation and measurement shows the value of 0.08 due to shock. Larger values of about 0.1 were measured just downstream of the Mach disk.

TKE takes on very low values, as it should, in the undisturbed part of the incoming flow and outside the bow shock. In the experiments, inflow levels were not too low (about 0.02) and even appeared near the upper wall. In the computations, the initial rise through the separation shock is to about 0.005 only. These levels are not sensitive to the specified freestream turbulence levels. In the experiments, the TKE distribution has a wavy structure along the jet as it develops downstream. These are likely to be due to some large-scale unsteadiness, possibly flapping, which is absent in the computations.

Generally, regions where TKE levels were low may not be comparable due to unsteadiness in the experiment, but the higher levels, which are consistent with turbulence generated at shear layers, have been quite accurately obtained.

Jet Development

Downstream crossflow planes show the presence of the counter-rotating vortex pair and its growth. In the corresponding incompressible injection flow, the jet penetration is larger and hence the near-wall wake is well separated from the jet. Here, the distance is less, and more interaction is likely. The measurements in the two transverse planes $x = 3d$ and $x = 5d$ provide data about the development of the jet in the near field and far field. Data cover a region of height of 4 diameters and a half-span of 3.75 diameters

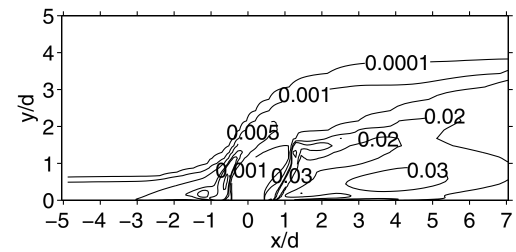

Fig. 8 Turbulence kinetic energy contours on symmetry plane ($z = 0$).

($0 < y < 4d$, $0 < z < 3.75d$). Measurements were made down to a distance of about 1 mm from the wall. Sample measurements [2] at different heights indicated that mean velocities were symmetric but fluctuations had some asymmetry in the $x = 3d$ plane.

Mean Velocities in the Near Field $x = 3d$

The dimensionless mean streamwise velocity u/U_∞ on the $x = 3d$ plane is shown in Fig. 9. Near the midplane, the upper structure is that of the jet, and the lower one is that of the wake. In the jet, a minimum streamwise velocity of about $u/U_\infty \approx 0.70$ was observed in the experiment at a height of $y/d = 1.5$ on the symmetry plane. The computation predicted a lower value of around 0.5. In the experiments, streamwise velocity values increased uniformly outward from the low value region to the outer freestream level, with an annular shear layer. In the computations, this shear layer is slightly distorted. In the region between the jet and the wall and close to the symmetry plane ($y \approx 0.7d$, $z \approx 0.2d$), a fairly large value of about 0.8 was measured. Santiago and Dutton [2] noted that crossflow fluid might have entered this region and could also be mixed with jet fluid quickly due to entrainment by the counter-rotating vortices. The computation also shows similar levels of about 0.8 in this region, but the minimum value (about 0.6 on the symmetry plane) is again lower than that (about 0.8) in the experiment. The incoming flat plate boundary layer thickness is a little less than d. Injection has disrupted this boundary layer, and at $x = 3d$, the part of the boundary layer that does not mix with the injection flow lies outside z/d of about 3.5 in the experiment and a little closer in the computation.

The wall-normal component (v/U_∞) (Fig. 9b) is positive where the jet moves upwards, with higher values on the top boundary and lower ones below, and peak levels in between correspond to the entrainment flow between the streamwise vortices. Outside this, there is a pocket of negative levels, again consistent with the action of the streamwise vortex. The shapes of these regions are slightly different in experiment and computation, especially the outer flow toward the plate. A maximum value of about 0.45 was measured at a height of about 1.4 diameters near the symmetry plane. Simulation levels are higher, about 0.7 at about the same location. But, higher levels were measured in the regions away from the jet where the wall-normal velocities should be small.

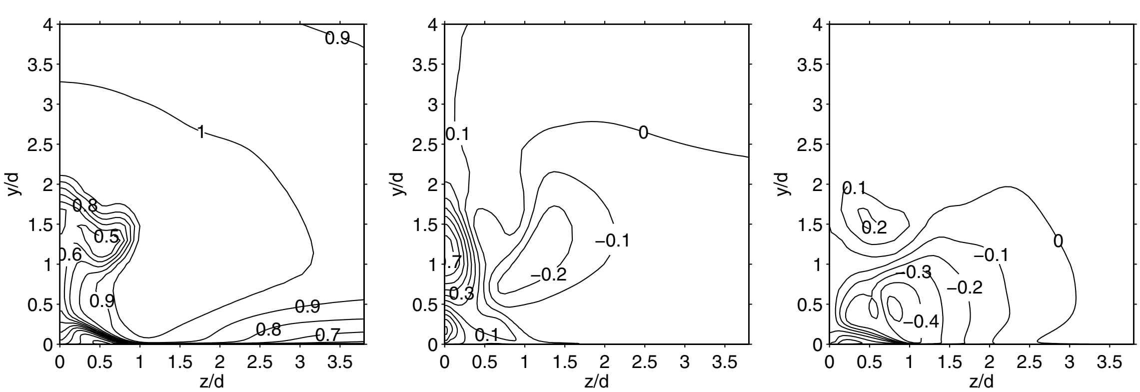

a) b) c)

Fig. 9 Mean velocities at $x = 3d$. a) (u/U_∞); b) (v/U_∞); c) (w/U_∞).

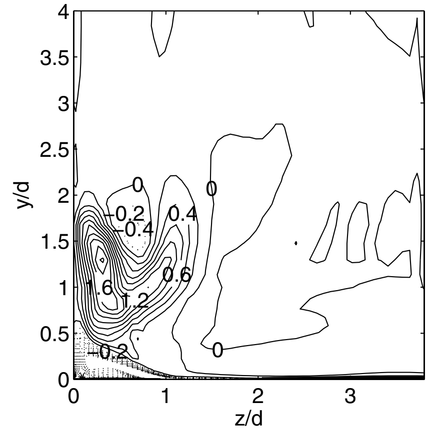

Fig. 10 Mean streamwise vorticity $\zeta_x d/U_\infty$ in crossflow plane at $x = 3d$, Solid line: $\zeta_x \geq 0$; dashed line: $\zeta_x < 0$. Second-order scheme used.

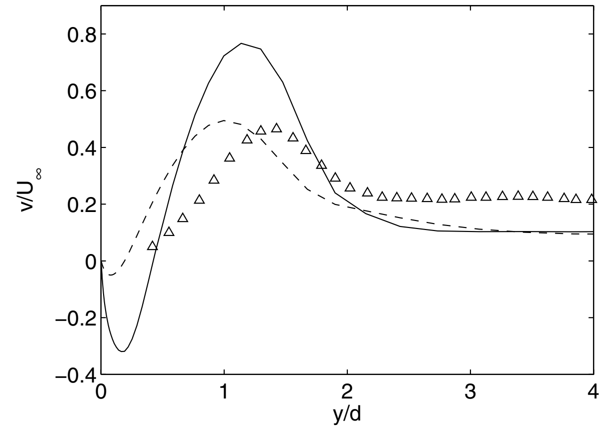

Fig. 11 Upwash velocity on symmetry plane at $x = 3d$. Solid line: second-order scheme; dashed line: first-order scheme; △: experiment [2].

The spanwise velocity (Fig. 9c) is essentially the flow induced by the streamwise vorticity of the jet. So there are positive values at a height of about $1.5d$ of the outward flow and negative values close to the wall where the flow comes in toward the symmetry plane. There is closer agreement of the magnitudes, if not of the distribution, with the experiment.

The dimensionless mean streamwise vorticity

$$\frac{\zeta_x}{U_\infty/d} = \frac{d}{c}\left[\frac{\partial w}{\partial y} - \frac{\partial v}{\partial z}\right]$$

at $x = 3d$ is shown in Fig. 10. The jet's crossflow vortices lie over wall vortices. Because measurements were not taken close to the wall, these wall vortices were not seen in the plot from the experiment. As discussed here, the computed velocity field agrees reasonably well with experiments, but differences are observed in vorticity distributions. For example, the experiments showed only positive vorticity in the jet region. The computation shows a pocket of negative vorticity nestled between regions of positive vorticity on the upper part of the jet. Peak vortex strength is also about double that in the experiment. We note here that a first-order scheme diffuses the jet structure so that the region of negative vorticity (in the jet) is not captured giving a distribution that is closer to the experiment. Both second- and third-order schemes give similar solutions. Circulation strength is almost same in all three solutions. These differences can be seen in a plot of upwash velocity on the symmetry plane at $x = 3d$ (Fig. 11). Note that the first-order solution is closer to the experiment, whereas the higher-order solution has sharper gradients and also larger magnitudes.

Turbulence Quantities in the Near Field $x = 3d$

In the computation, turbulence kinetic energy is high in the regions of high strain rates between the jet and the wall layer vortices. In the experiment, the TKE in the jet plume is about 0.054 and is about 0.005 in the far fields [2]. The computation shows peaks of about 0.016 in the jet, in two regions like the vorticity field (Fig. 12a).

Figure 12b shows the Reynolds shear stress component $\langle u'v'\rangle/U_\infty^2$ at $x = 3d$. Peak levels in the experiment are significantly higher (about -0.012 in the jet), but the distributions of positive and negative values are similar. Significant levels were present in the experiment outside and above the jet, which may be due to unsteadiness. The other component $\langle u'w'\rangle/U_\infty^2$ is plotted in Fig. 12c. Peak levels in the experiment were higher (-0.02) in the jet's outer boundaries, but small levels were present everywhere.

Features at $x = 5d$

In the experiment, most of the general characteristics of the mean and fluctuating fields of the crossflow at $x = 5d$ plane are similar to those of the $x = 3d$ plane. The annular shear layer grew significantly in the transverse direction but had barely changed in the spanwise direction. Because qualitative aspects of flow structure in the $x = 5d$ plane are close to those in the $x = 3d$ plane, and the comparisons of velocity distributions in the $x = 3d$ plane have been presented in detail, here, the vorticity contours alone have been compared (Fig. 13). In the computation, once again the jet plume contains a small, weak pocket of vorticity of opposite sense. The streamlines also show a single recirculation center at $x = 3d$. The center of the closed streamlines ($y = 1.4d$, $z = 0.59d$) is close to those in the experiment ($y = 1.38d$, $z = 0.63d$).

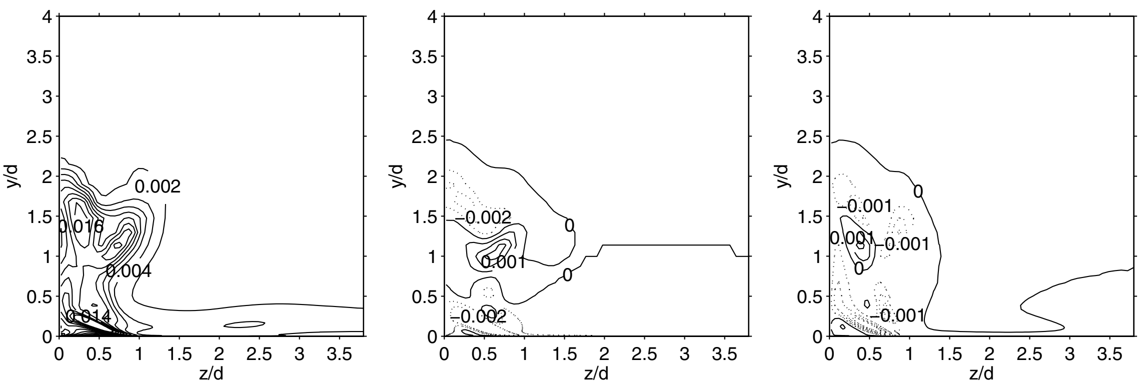

Fig. 12 Mean turbulence quantities in crossflow plane at $x = 3d$. a) turbulence kinetic energy; b) Reynolds shear stress ($\langle u'v'\rangle/U_\infty^2$); c) Reynolds shear stress ($\langle u'w'\rangle/U_\infty^2$).

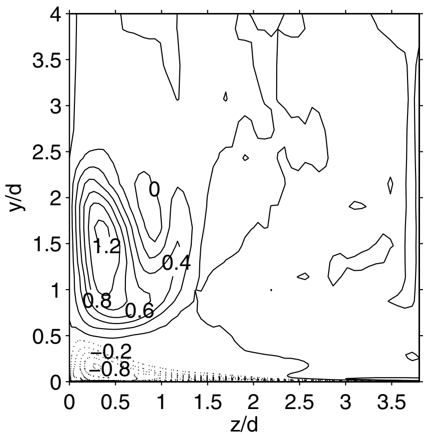

Fig. 13 Mean streamwise vorticity $\zeta_x d/U_\infty$ in crossflow plane at $x = 5d$. Solid line: $\zeta_x \geq 0$; dashed line: $\zeta_x < 0$.

Peak values of TKE decreased slightly from 0.054 at $x = 3d$ to 0.051 at $x = 5d$ in the experiment. In the computation, the maximum value decreased from about 0.016 to 0.014. The Reynolds shear stress component $\langle u'v' \rangle / U_\infty^2$ had the local minimum near the top of the jet plume (at the $z = 0$ centerline) and $y = 2.38$ had decreased slightly (in magnitude) to a value of -0.013 from -0.014 at $x = 3d$. This is confined to a very small region, and the level increases gradually to 0.002. The computation shows a minimum of -0.001 in the region, where the experiment had a range of negative values down to -0.012. Both experiment and computation show a region of negative values beneath of jet plume. There are differences in structures of the distributions of Reynolds shear stress component $\langle u'w' \rangle / U_\infty^2$, but the levels are quite small.

Flow Features on the Wall

The computed pressure distribution over one-half of the wall is shown in Fig. 14. The foot of the curved bow shock, the lateral extend of the separation shock, a low pressure region in the wake region and the adjustment of pressures in various regions are evident. These distributions agree well with pictures of PSP visualization of this flow [7]. Generally, the curve of upstream separation is closer to the jet in computations. The difference is largest on the symmetry plane (see Figs. 5 and 6), but not as much in the spanwise direction. The foot of the bow shock stands very close to the injection port and extends about $2d$ in the spanwise direction. Peak pressure rise, at the center portion of the foot of the bow shock, is about twice the freestream pressure. Its value changes little with injection pressure [7,27], but is strongly influenced by inflow Mach number.

A qualitative description of the flow near the wall was provided as sketches of the oil flow patterns indicating separation lines and points of accumulation [2]. A useful comparison of these oil flow sketches is with tangent lines of the shear stress vector field on the plate. Shear stress components are

$$\tau_{yx} = \frac{\partial u}{\partial y} + \frac{\partial v}{\partial x}, \qquad \tau_{yz} = \frac{\partial w}{\partial y} + \frac{\partial v}{\partial z}$$

Because the velocity vanishes everywhere on the wall, only the wall-normal derivative is nonzero. A second consequence is that, to leading order, the stress vector is proportional to the projection of the velocity vector at a plane parallel to the wall on this same plane. We take this plane to be where the first grid points off the wall are located. The error is then $\mathcal{O}(\Delta y)^2$. Several streamlines of this wall-parallel velocity field (or tangent lines of the wall shear stress vector field) are shown in Fig. 15. We find these tangent lines and the oil flow curves [2] (though sketched) to have remarkably similar shapes.

When the mean field computations are reasonably accurate, the solutions can be used to examine flow features to meet design requirements. The present flow is a basic configuration for supersonic combustion where the distances required for mixing are important. As an example, Fig. 16 shows some pathlines beginning

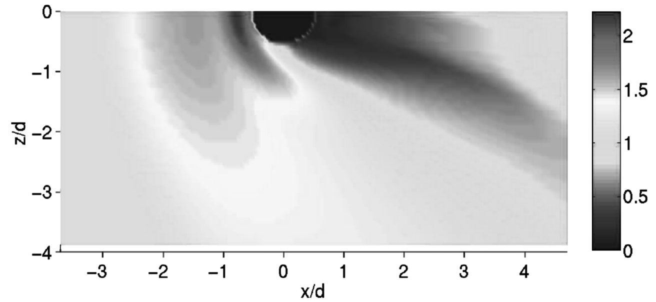

Fig. 14 Wall pressure distribution from computation for case 1 of Table 1.

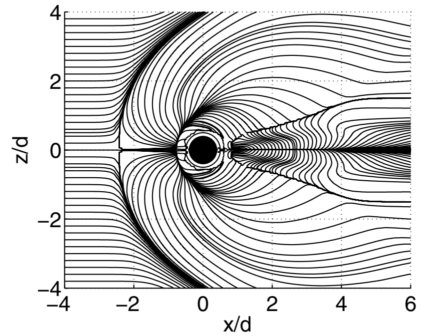

Fig. 15 Tangent lines of wall shear stress vector field from computation for case 1 of Table 1.

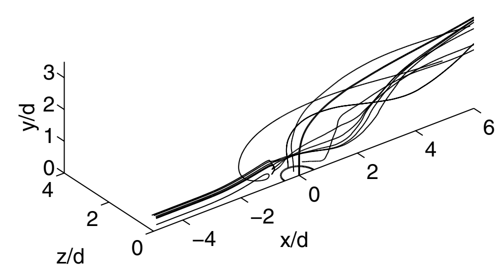

Fig. 16 Path lines of particles from the upstream boundary layer and through the injector for case 1 of Table 1.

within the incoming crossflow boundary layer. These lines lift up at the first separation, drop down very close to the wall, curve around the jet, and enter the jet from below. A particle that is closer to the wall in the upstream boundary layer travels farther spanward before entering the jet. Also shown are three pathlines originating at the injector plane, one at the hole center, one at the periphery, and one in between. The helical paths taken by the pathlines in the jet are seen. Such plots reveal, for example, the distance traveled (on the average) by jet fluid packets around the periphery before entering the core. Such information becomes useful after it is established that calculations such as the present ones are accurate.

Simulation of Experiments of Aso et–al.

Cases 5–7 of Table 1 are the experiments of Aso et al. [10] conducted at higher a significantly higher Mach number. Wall pressure from several ports located around the injector was reported. These ports were arranged in lines aligned with the stream, and the lines were at spanwise distances $z/d = 0, 1, 2, 3, 4, 5$. Data from the present simulations and experiment have been plotted in Fig. 17 for the highest pressure ratios $p_{\text{jet}}/p_\infty = 26.29$ at each of the spanwise stations. All predictions were comparable with experiments except those at $z/d = 4$. This discrepancy is due to the different rate at which the horseshoe vortices wrap around the jet, and so the kink that appears at a certain span in the experiment may appear at a slightly

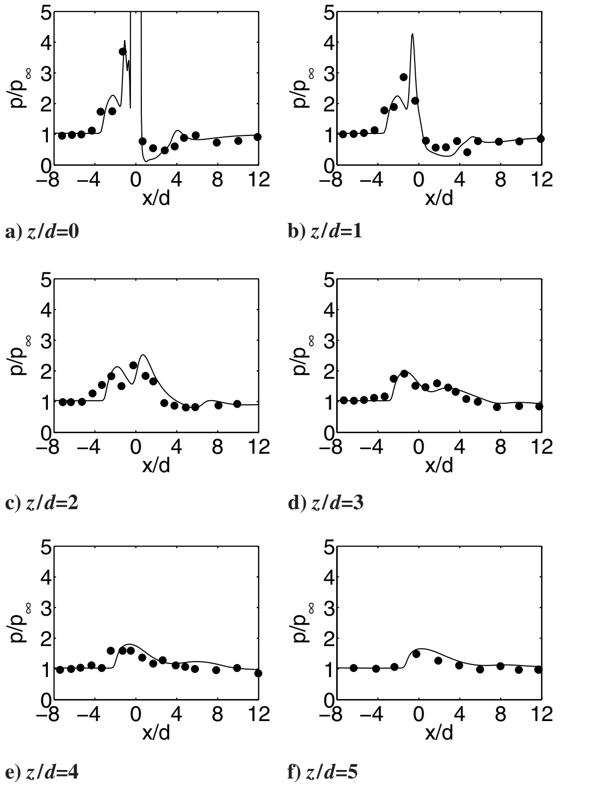

Fig. 17 Wall pressures for $p_{\text{jet}}/p_\infty = 26.29$, $M_\infty = 3.75$, and $d = 5$ mm (case 7 from Table 1). ●: experiment; solid line: computation.

different location in the computation. The small oscillation present at $z = 2d$ is comparable to that in the experiment.

Sketches of their oil flow patterns were also provided. Figure 18 shows the tangent lines of the wall shear stress from our simulations. As the injection pressure ratio is increased from 8.57 to 17.72, the tangent line pattern remains similar. The differences are quantitative, such as the increased spanwise extent of the separated flow. However, with further increase to 26.29, there is a qualitative change in flow structure downstream of the port as an additional nested separation zone appears. We note that there is good agreement with the oil flow visualization [10], especially of this structural change with increased injection pressure, and of the location of bounding lines between different zones. There are some differences in the precise shapes and alignments of the tangent lines within the different zones. We note that these were *sketches* of the oil flow and were a small part of the efforts in the experiments. Although the presence and the appearance of new separation zones at higher injection pressures are interesting, no previous simulations have examined these in detail. The present examination was motivated by attempts to check the correctness of the solutions. We had found that the nested separations were not obtained in the first-order solutions.

Conclusions

Numerical simulations have been performed of the transverse injection of sonic jets into supersonic crossflows. Two sets of wind tunnel experiments have been selected to test the accuracy of numerical predictions. Various numerical aspects such as grid dependence, convergence, and effects of scheme order were examined. The solution with higher-order schemes showed a secondary vortex as the jet developed downstream. Also, higher-order schemes are necessary to capture the nested separation visualized in higher injection pressure experiments.

From the comparisons with the LDV data, we find that the region upstream and near the injector are in good quantitative agreement, whereas downstream, the quantitative agreement is not as good because the jet evolves at different rates in the experiment and simulation.

On the symmetry plane, the main features, such as location of Mach disk, separation shock, and bow shock, were predicted well. In the experiment, turbulent kinetic energy had very low values at the core of initial portion of emerging jet, almost like an inviscid core, and high values in the shear layers and at the Mach disk. Turbulence amplification occurs across shocks. These features are captured in the computation. Unlike the computation, the experiment had a wavy distribution of TKE in the downstream jet, which could be due to large-scale unsteadiness.

The important feature of counter-rotating vortices in the evolving jet has been simulated. Though the computation shows good qualitative and quantitative agreement with measured distribution of velocity components, higher-order quantities like vorticity show some differences. Computation showed the presence of additional vorticity in the opposite sense, but the strength of circulation is comparable with experiments. It is also seen that the strength of the additional vortex reduces downstream. The presence of the additional vortex is a sensitive feature for computations because the first-order scheme was unable to capture it. Future measurements in crossflow planes close to the jet injector that can resolve this feature would be helpful.

Wall pressure distributions on the symmetry line agree well with measurements. Measurements at various spanwise stations showed a pressure well and hump, which have been obtained in computations with higher-order schemes.

Tangent lines of the wall shear stress field from computations were compared with sketches of oil flow patterns from experiments. Sketches showed the upstream separation, a point on either side of the jet where oil coiled around/accumulated, and a divergent portion in the wake. Similar structures were obtained in the simulation. Features at the higher Mach number experiments were slightly different, showing interesting multiple separations with increasing the injection pressure. Computations with a higher-order scheme reproduced this nested structure. It is interesting that the patterns are different for similar momentum flux ratios (case no. 1 and case no. 7 of Table 1), but with considerably different crossflow Mach numbers.

We think it will be useful to conduct a closer simulation of this flow as a large eddy simulation that focuses on the development of the jet in the vicinity of the injector. Also, general studies of the near

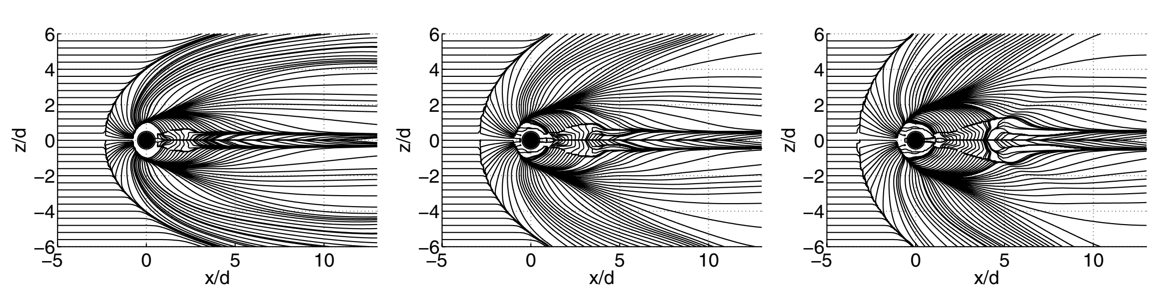

Fig. 18 Effect of injection pressure on tangent lines of wall shear stress vector field ($M_\infty = 3.75$ and $d = 5$ mm), cases 5–7 of Table 1.

wake, especially of the appearance of nested separated flows, will be useful as basic understanding and perhaps for designing better scramjet combustors.

Acknowledgments

We thank J. C. Dutton and J. G. Santiago for readily sending us their experimental data and for useful discussions. The first author acknowledges financial support for a part of this work from the AR&DB Centre of Excellence for Aerospace CFD at the Indian Institute of Science.

References

[1] Santiago, J. G., and Dutton, J. C., "Velocity Measurements of a Jet Injected into a Supersonic Crossflow," *Journal of Propulsion and Power*, Vol. 13, No. 2, 1997, pp. 264–273.
[2] Santiago, J. G., and Dutton, J. C., "An Experimental Study of the Velocity Field of a Transverse Jet Injected into a Supersonic Crossflow," University of Illinois at Urbana–Champaign, TR UILU-ENG 95-4047, 1995.
[3] Zukoski, E. E., and Spaid, F. W., "Secondary Injection of Gases into a Supersonic Flow," *AIAA Journal*, Vol. 2, No. 10, 1964, pp. 1689–1696.
[4] Hawkins, P. F., Lehman, H., and Schetz, J. A., "Structure of Highly Underexpanded Transverse Jet in a Supersonic Stream," *AIAA Journal*, Vol. 5, No. 5, 1968, pp. 882–884.
[5] Gruber, M. R., Nejad, A. S., Chen, T. H., and Dutton, J. C., "Mixing and Penetration Studies of Sonic Jets in a Mach 2 Freestream," *Journal of Propulsion and Power*, Vol. 11, No. 2, 1995, pp. 315–323.
[6] Santiago, J. G., and Dutton, J. C., "Crossflow Vortices of a Jet Injected into a Supersonic Crossflow," *AIAA Journal*, Vol. 35, No. 5, 1997, pp. 915–917.
[7] Everett, D. E., Woodmansee, M. A., Dutton, J. C., and Morris, M. J., "Wall Pressure Measurements for a Sonic Jet Injected Transversely into a Supersonic Crossflow," *Journal of Propulsion and Power*, Vol. 14, No. 6, 1998, pp. 861–868.
[8] Gruber, M. R., Nejad, A. S., Chen, T. H., and Dutton, J. C., "Bow Shock/Jet Interaction in Compressible Transverse Injection Flowfields," *AIAA Journal*, Vol. 34, No. 10, 1996, pp. 2191–2193.
[9] Gruber, M. R., Nejad, A. S., Chen, T. H., and Dutton, J. C., "Compressibility Effects in Supersonic Transverse Injection Flowfields," *Physics of Fluids*, Vol. 9, No. 5, 1997, pp. 1448–1461. doi:10.1063/1.869257
[10] Aso, S., Okuyama, S., Ando, Y., and Fujimori, T., "Two-Dimensional and Three-Dimensional Mixing Flowfields in Supersonic Flow Induced by Injected Secondary Flows Through Transverse Slot and Circular Nozzle," AIAA Paper 93-0489, 1993.
[11] Drummond, J. P., "Supersonic Reacting Internal Flowfields," *Progress in Astronautics and Aeronautics*, Vol. 137, 1991, pp. 365–420.
[12] Segal, C., Haj-Hariri, H., and McDaniel, J. C., "A Numerical Investigation of Hydrogen Combustion in Mach 2 Airflow," AIAA Paper 92-0341, 1992.
[13] Mao, M., Riggins, D. W., and McClinton, C. R., "Numerical Simulation of Transverse Fuel Injection," *Computational Fluid Dynamics Symposium on Aeropropulsion*, NASA CP-1386, 1990, pp. 635–667.
[14] McDaniel, J. C., and Graves, J., Jr., "Laser-Indused-Fluorescence Visualisation of Transverse Gaseous Injection in a Nonreacting Supersonic Combustor," *Journal of Propulsion and Power*, Vol. 4, No. 6, 1988, pp. 591–597.
[15] Uenishi, K., and Rogers, R. C., "Three-Dimensional Computation of Mixing of Transverse Injector in a Ducted Supersonic Airstream," AIAA Paper 86-1423, 1986.
[16] Aso, S., Tannou, M., Maekawa, S., Okuyama, S., Ando, Y., Yamane, Y., and Fukuda, M., "A Study on Mixing Phenomena in Three-Dimensional Supersonic Flow with Circular Injection," AIAA Paper 94-0707, 1994.
[17] Maddalena, L., Campioli, T. L., and Schetz, J. A., "Experimental and Computational Investigation of Light-Gas Injectors in Mach 4.0 Crossflow," *Journal of Propulsion and Power*, Vol. 22, No. 5, 2006, pp. 1027–1038.
[18] Sriram, A. T., and Mathew, J., "Improved Prediction of Plane Transverse Jets in Supersonic Crossflows," *AIAA Journal*, Vol. 44, No. 2, 2006, pp. 405–408.
[19] Sun, C., and Childs, M. E., "A Modified Wall Wake Velocity Profile for Turbulent Compressible Boundary Layers," *Journal of Aircraft*, Vol. 10, No. 6, 1973, pp. 381–383.
[20] Wilcox, D. C., *Turbulence Modeling for CFD*, DCW Industries, Inc., La Cañada, CA, 1993.
[21] Sarkar, S., Erlebacher, G., Hussaini, M. Y., and Kreiss, H. O., "The Analysis and Modelling of Dilatational Terms in Compressible Turbulence," *Journal of Fluid Mechanics*, Vol. 227, 1991, pp. 473–493. doi:10.1017/S0022112091000204
[22] Zeman, O., "Dilatation Dissipation: The Concept and Application in Modelling Compressible Mixing Layers," *Physics of Fluids A*, Vol. 2, No. 2, 1990, pp. 178–188. doi:10.1063/1.857767
[23] Hirsch, C., *Numerical Computation of Internal and External Flows*, Vol. 2, Wiley, New York, 1990.
[24] Bussing, T. R. A., and Murman, E. M., "Finite-Volume Method for the Calculation of Compressible Chemically Reacting Flows," *AIAA Journal*, Vol. 26, No. 9, 1988, pp. 1070–1078.
[25] Gerlinger, P., Algermissen, J., and Bruggemann, D., "Numerical Simulation of Mixing for Turbulent Slot Injection," *AIAA Journal*, Vol. 34, No. 1, 1996, pp. 73–78.
[26] Anderson, D. A., Tannehill, J. C., and Pletcher, R. H., *Computational Fluid Mechanics and Heat Transfer*, Hemisphere, Washington, D.C., 1984.
[27] Sriram, A. T., "Numerical Simulations of Transverse Injection of Plane and Circular, Sonic Jets into Turbulent, Supersonic Crossflows," Ph.D. Thesis, Department of Aerospace Engineering, Indian Institute of Science, Bangalore, India, 2003.

J. Oefelein
Associate Editor